ACS Photonics

pubs.acs.org/journal/apchd5

Article

Room-Temperature Fiber Tip Nanoscale Optomechanical Bolometer

Shen Liu, Yanping Chen, Huailei Lai, Mengqiang Zou, Hang Xiao, Peijing Chen, Bin Du, Xunzhou Xiao, Jun He, and Yiping Wang*

Cite This: *ACS Photonics* 2022, 9, 1586−1593

Read Online

ACCESS | Metrics & More | Article Recommendations | Supporting Information

ABSTRACT: Nanomechanical bolometers have proven to be well suited to the analysis of light. However, conventional wafer-based devices have limited practical applications because they require special vacuum chambers, cryogenic temperatures, bulky space optical components, and/or complex circuitry. The present work developed a nanoscale optomechanical bolometer intended for photothermal sensing using an all-optical actuation and measurement approach. The proposed bolometer is compact and has an integrated all-optical-fiber structure based on fabricating a Fabry−Perot interferometer incorporating multilayer graphene at the fiber tip and packaged in a small vacuum-sealed tube. This microscale vacuum packaging doubled the signal-to-noise ratio compared with that in air. This miniature all-fiber nanoscale optomechanical bolometer also exhibited a high resolution with photothermal sensitivities of approximately 6.23 and 6.44 kHz/μW when using the second-order mode at room temperature and 0 °C, respectively. This design could be beneficial for applications outside specialized laboratories with uses in the fields of medicine, industrial manufacturing, nanoscience, and astronomy.

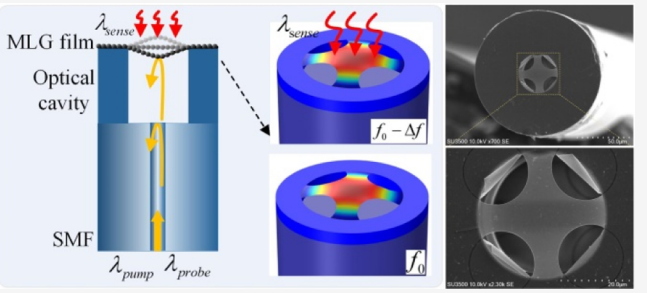

KEYWORDS: *nano-optomechanical, graphene, micro-vacuum package, micro-bolometer, room temperature*

INTRODUCTION

In recent years, various nano-electromechanical systems (NEMSs) have been developed based on suspended nanoscale objects, such as nanowires,[1−3] graphene,[4−9] MoS_2 films,[10,11] $MoSe_2$ films,[12] and nanotubes.[13−15] These NEMS-based resonators have been used to fabricate high-performance sensors capable of measuring force,[9] mass,[10,16,17] thermal radiation,[3,12,18,19] current,[20] pressure,[21] and magnetic fields[22,23] while providing the advantage of having ultrasmall masses. Graphene, a material comprising sheets made of single atomic layers and exhibiting high stiffness, low mass, and good thermal conductivity along the basal plane, is an ideal candidate for the fabrication of nano-optomechanical resonators and nanomechanical resonators. Bunch et al.[24] fabricated the first NEMS resonator by transferring single or multiple graphene layers onto silicon oxide and examined the fundamental frequencies of these devices. The results indicated the feasibility of fabricating graphene-based resonators. Since then, a variety of suspended resonators based on single, a few, or multiple graphene layers have been reported. These devices have assisted in analyzing chemical or biological samples on the nanoscale.

Graphene exhibits absorbance over an extremely wide spectral range, has the lowest heat capacity per unit area of any material, and is thermally stable to above 2600 K. Thus, this material has the potential to allow for ultrasensitive and ultrafast bolometry.[25] Nevertheless, graphene has actually performed poorly to date in conventional bolometry systems[26] because electrical resistance is typically used to assess the power absorbed by the measurement device. However, resistance is relatively insensitive to temperature and the direct current transport readout of resistance-based devices is slow. It should be noted that graphene has performed well in hot-electron bolometry,[14,27] in which microwave frequency Johnson noise is used as a readout, working at telecom wavelengths. However, in such systems, a thermally insulated electron gas having a low electronic heat capacity is produced as a consequence of a weak electron−phonon interaction, and so, the sensitivity of the device is reduced at temperatures of 300 K or higher. Thus, cryogenic temperatures[28,29] are usually necessary for high sensitivity bolometry. The use of an optical readout has been considered as a means of addressing these issues because this approach provides high precision with ultrafast responses and is immune to electromagnetic interference. Blaikie et al.[6] proposed patterning a circular graphene drumhead into a trampoline geometry and used an optical readout to assess the thermal radiation at room temperature, where electrostatic actuators have been applied.

Received: October 31, 2021
Published: March 10, 2022

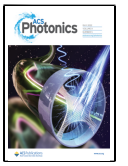

https://doi.org/10.1021/acsphotonics.1c01676
ACS Photonics 2022, 9, 1586−1593

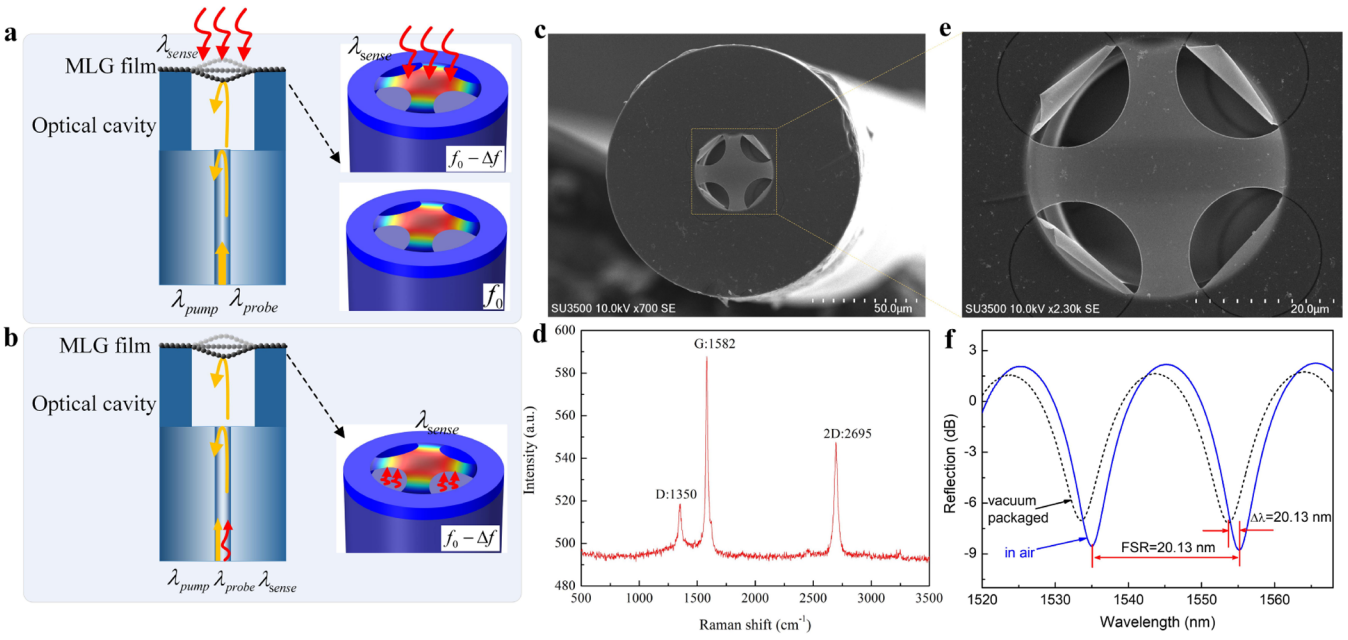

Figure 1. Diagrams, images, and properties of the present graphene resonators. Diagrams of a fiber-tip NOMS resonator receiving (a) external incident radiation and (b) internal incident radiation. (c) SEM image of a suspended graphene fiber tip having a trampoline morphology. (d) Raman spectrum of the graphene, exhibited a G mode peak at 1582 cm^{-1}. (e) Enlarged SEM image providing a partial view of the suspended graphene. (f) Typical reflection spectra obtained from the MLG-based fiber tip NOMS resonator before and after micro-vacuum packaging.

Electrostatic actuators have the limitation of using on-chip electronics that could degrade at high temperatures, although electrostatic actuators have been adopted for many graphene NEMS.[30] Furthermore, the careful alignment of bulky optical components is required for this type of bolometer, and a vacuum chamber is necessary for all the aforementioned graphene-based NEMS. For these reasons, standard graphene-based bolometers are presently used solely in laboratory settings because of the requirement for a vacuum chamber and/or complex demodulation systems that greatly restrict practical real-world applications.

The present work developed an all-fiber graphene nano-mechanical bolometer (GNB) system that is both portable and practical. This study involved the fabrication of a new type of fiber tip nano-optomechanical cavity-based resonator based on patterning graphene into a trampoline geometry using a focused ion beam (FIB) that was subsequently micro-vacuum packaged within a small, sealed tube. This device, demonstrated here for the first time, is applicable to photothermal sensing and spectroscopy at room temperature. This resonator, which we refer to as a fiber tip nano-optomechanical system (NOMS), is actuated by an intensity-modulated pump laser that excites mechanical resonance and is read out using a probe laser. The air damping effect is significantly reduced in the case of this technique and the signal-to-noise ratio (SNR) obtained using the micro-vacuum packaging is almost doubled compared with that in air. The resonant frequency of the suspended graphene in this device will vary as a consequence of even a small degree of light absorption, which creates thermal tension. By measuring absorption-induced frequency shifts, a photothermal sensitivity of approximately 2.18 kHz/μW was achieved at room temperature when monitoring the first-order fundamental mechanical frequency. Sensitivities of 6.23 and 6.44 kHz/μW were achieved using the second order mode at room temperature and at 0 °C, respectively. Furthermore, the absorbed power could originate from either outside or inside the device. Data for the device with a 40 μm diameter trampoline is presented herein. This new type of sensor platform based on absorption spectroscopy has the advantages of being fabricated solely from integrated optical fibers and having all-optical actuation and measurement components that are immune to electromagnetic interference.

RESULTS AND DISCUSSION

Figure 1 presents a schematic of a NOMS-based fiber-tip bolometer with a multilayer graphene (MLG) film. An intensity-modulated pump laser (λ_{pump}) and a probe laser (λ_{probe}) are used to actuate this MLG film and to detect the mechanical vibrations induced in the device, respectively (see Supporting Information Methods). The absorbed light can originate external to the device, as shown in Figure 1a, or can be internal, as shown in Figure 1b. Any incident radiation (λ_{sense}) will be absorbed such that the temperature of the MLG film is increased, resulting in thermo-mechanical stress that shifts the resonant frequency by Δf according to the equation[6]

$$\Delta f = \frac{\alpha Y f_0}{2\sigma_0(1-\nu)}\Delta T \tag{1}$$

Here, α, ν, and σ_0 are the thermal expansion coefficient, Poisson ratio, and initial in-plane stress, respectively, while f_0, Y, and ΔT are the initial frequency, the two-dimensional elastic modulus, and the temperature rise, respectively. The temperature rise increases as the absorbed optical power increases, and is calculated as[31]

$$\Delta T = \frac{P_{absorbed}\tau_{thermal}}{C_p m} \tag{2}$$

where, C_p, m, $P_{absorbed}$, and $\tau_{thermal}$ are the specific heat, the mass of the MLG film, the absorbed optical power, and the thermal time constant, respectively.

https://doi.org/10.1021/acsphotonics.1c01676
ACS Photonics 2022, 9, 1586−1593

Figure 1c shows a typical scanning electron microscopy (SEM, SU3500) image of the fiber tip graphene-based NOMS resonator. A circular drumhead-style graphene resonator was obtained by directly transferring graphene onto a fiber tip having an open micro-cavity. The drumhead was subsequently patterned into a trampoline geometry using a FIB technique (see Methods for details). An enlarged SEM image of the graphene resonator is shown in Figure 1e and demonstrates good uniformity throughout the graphene specimen. Figure 1d presents the Raman spectrum obtained from the graphene after transferring to the fiber tip, which exhibits a G mode peak at 1582 cm^{-1}.

The MLG film and the fiber end face form a low-finesse Fabry–Perot (FP) cavity interferometer. The actual cavity length in this device can be calculated from its reflection spectrum (see Supporting Information Methods for details). Figure 1f provides typical reflection spectra acquired from a resonator before and after micro-vacuum packaging. The interference fringe contrast in these images is approximately 11 dB as a result of the large reflectivity of the stacked MLG, and a large cavity length of approximately 60 μm. In the present experiments, the cavity length varied from sample to sample but the fringe contrast in the interference patterns was sufficiently large for demodulation (varying from approximately 10 dB to over 25 dB). Notably, this contrast value increased as the cavity length decreased, as a consequence of the transmission loss of light reflected by the MLG film, decreased along with decreases in the cavity length. As noted, the present GNB was micro-vacuum packaged so that it was unaffected by the movement of ambient air while minimizing air damping. Consequently, a high SNR was achieved. The reflectance spectrum obtained after applying the vacuum packaging demonstrates a slight blue shift and a small decrease in the extinction ratio, possibly because the flatness of the film was changed by applying a vacuum.

Mechanical Property Measurements. The frequency spectra of the resonator and the noise spectral density of the device were assessed using the optomechanical system shown in Figure S1a (see the Supporting Information). The frequency spectrum of the resonator was acquired both in air and in the micro-vacuum package with a constant pump power and probe power. As shown by the dark solid curve in Figure 2a, the spectrum obtained in air exhibited resonance peaks at 4.39 and 4.13 mV, corresponding to frequencies of 602.78 and 1319.57 kHz, respectively. However, after the resonator was micro-vacuum packaged, three peaks appeared at higher energies of 8.31, 2.98, and 10.49 mV, corresponding to 612.61, 787.08, and 1347.55 kHz, respectively (dark gray solid line in Figure 2a). The light gray solid line shown in Figure 2a is the electrical noise from the electronics in the demodulation system as measured with both pump and probe power turned off. The red solid and blue short-dashed lines are the fitting results for the experimental data. The three resonance frequencies generated by the micro-vacuum packaged device also exhibited amplitudes that were nearly twice those of the peaks obtained from the specimen in air. The peak at 787.08 kHz can possibly be attributed to the imperfect edges of the MLG film or to edge/transverse modes resulting from nonuniform strain.[32] This peak was not evident in the air spectrum but was intense in the micro-vacuum spectrum. We attribute this result to the damping effect of air on the vibration of the diaphragm. Moreover, the resonator showed sharper resonance frequency peaks and lower shot noise following the

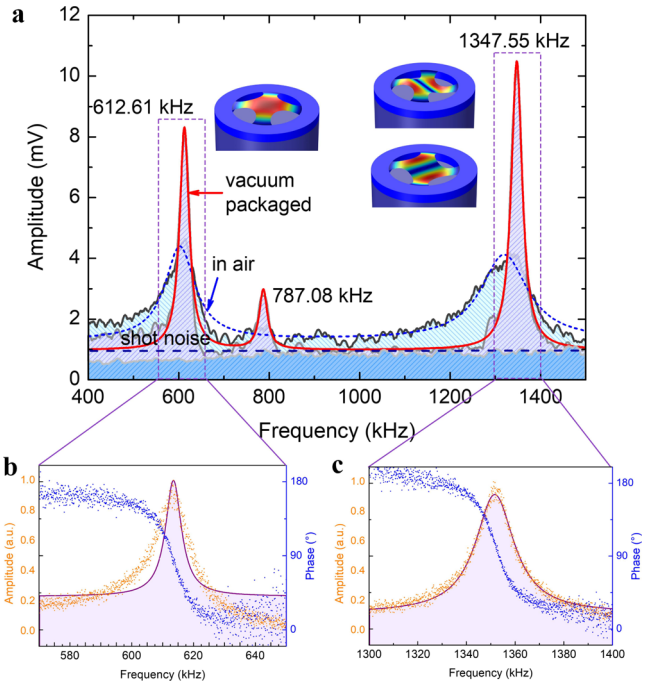

Figure 2. Amplitude and phase data for the response of the fiber tip NOMS resonator. (a) Amplitude versus frequency plots. The dark and dark gray solid plots indicate data acquired in air and in the micro-vacuum packaging, respectively. The light gray solid plot represents the electrical noise measured in the absence of probe and pump power. The blue short-dashed and red solid lines are the fitting results for the experimental data. The blue long-dashed line indicates the shot noise level. (b) Enlarged view of the amplitude and phase for first-order fundamental mechanical resonance. (c) Enlarged view of the amplitude and phase for second-order fundamental mechanical resonance.

micro-vacuum packaging, indicating that this was an effective approach to improve the SNR. The harmonic frequencies after micro-vacuum packaging were also shifted compared with those in air, which is attributed to the decrease in the pressure experience by the device from normal atmospheric pressure to 3.7×10^{-6} mbar. The peaks at 612.61 and 1347.55 kHz correspond to flapping and tilting mechanical resonance modes, respectively, as shown by the inset images to this figure (generated using COMSOL Multiphysics). The first-order and second-order frequencies were measured individually using an electronic network analyzer and the phase and amplitude spectra for these two modes are presented in Figure 2b,c, respectively. The amplitude responses for both the first order and the second order data have Lorentzian shapes, as expected for a harmonic oscillator with linear damping. The first-order fundamental resonance frequency was approximately 612.61 kHz with a quality factor of about 100. The phase responses of these two frequencies exhibited a shift of close to π rad, as expected for a pure harmonic resonator with no parasitic signals, indicating a linear response. This is the result of good decoupling between optical actuation and detection in the device.

Photothermal Sensing. The photothermal response of the resonator that produced the electrical spectrum shown in Figure 2a was assessed. As noted, in the present work, λ_{sense} equaled λ_{pump}, and the measured sensor signal originated internally, as shown in Figure 1b. All measurements were performed at room temperature and were within the

https://doi.org/10.1021/acsphotonics.1c01676
ACS Photonics 2022, 9, 1586–1593

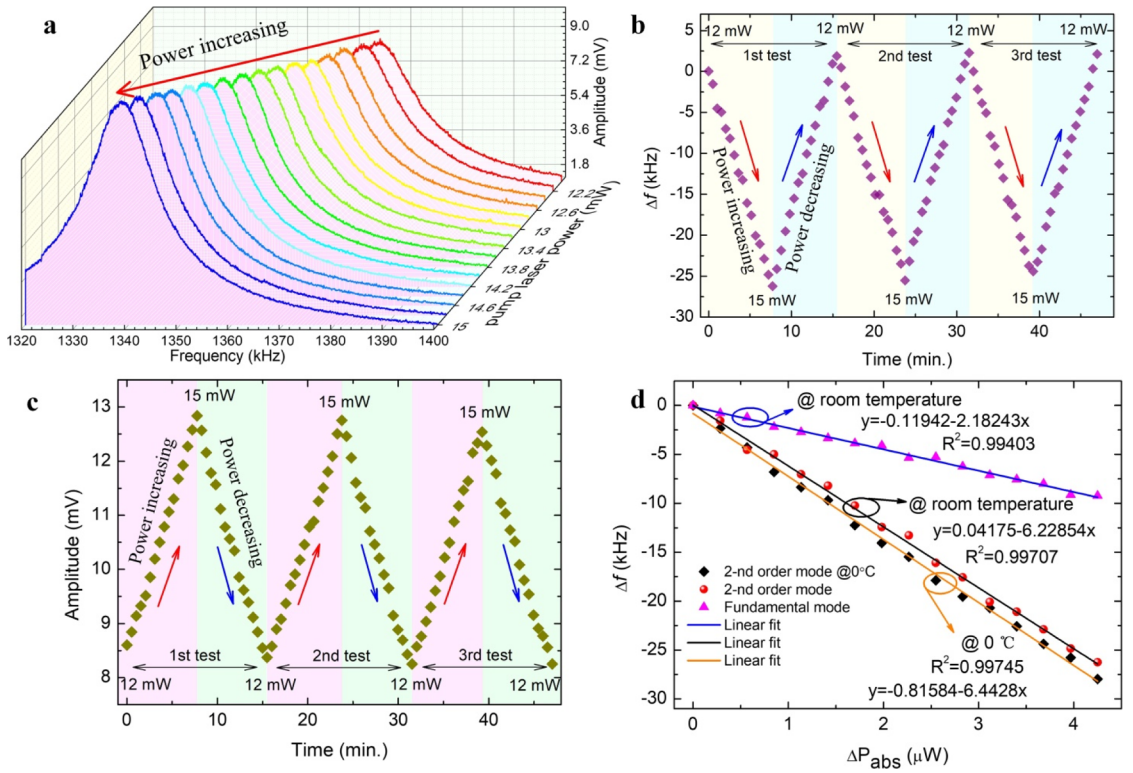

Figure 3. Photothermal sensing results. (a) Shift in the second-order mode resonance frequency of the NOMS, f_2, while increasing the pump power from 12 to 15 mW in steps of 0.2 mW. (b) Shifts in f_2 over time as different pump powers are applied to the MLG. (c) Variation of amplitude at f_2 as different pump powers are applied to the MLG. (d) Shift of the resonance frequency Δf as a function of absorbed laser power increase ΔP_{abs}.

resonator's linear working range. Figure 3a plots the evolution of the shift in the second-order resonance frequency, f_2, of the MLG resonator while the pump power is increased from 12 to 15 mW in increments of 0.2 mW at room temperature using λ_{probe} = 1530.2331 nm (3.551 mW) and λ_{pump} = 1549.0 nm. Each measurement was carried out with a time interval of 31 s to ensure that the pump power was stabilized. It is evident that the second-order frequency, f_2, was shifted to lower frequencies as the pump power was increased. Photothermal absorption compressed the NOMS structure and so reduced the total tensile strain, resulting in a decrease in the resonant frequency. Similar results were observed when monitoring the first fundamental mode resonance frequency as well (see Supporting Information, Note 1 for details).

The reproducibility of the bolometer was investigated by cycling the pump power between 12 and 15 mW in steps of 0.2 mW while keeping the other key parameters fixed. The shift in the second-order mode frequency (Δf) was plotted versus time, as shown in Figure 3b. In the three repeatability tests with increasing pump power, the resonant frequency was found to shift to lower frequencies by 26.24, 27.42, and 26.70 kHz, respectively. Resonant frequency shifts to higher frequencies were observed in cycling tests when the pump power was decreased. A similar frequency drift trend was observed during all three cycles. However, the frequency stability of the bolometer drifted during long-term trials (i.e., those lasting more than a few tens of minutes). We investigated the frequency stability of the NOMS resonator over time and described the frequency measurement error by the Allan deviation (see Supporting Information, Note 2).

The mechanical displacement amplitude at f_2 versus time is plotted in Figure 3c. In three repeatability tests during which increasing pump power was applied, the amplitude values increased by 4.23, 4.38, and 4.29 mV, respectively. Similar to the observed frequency shifts, the opposite variations in displacement amplitude at f_2 were obtained in cycling tests, in which the pump power was increased and then decreased. This effect can be attributed to the proportional relationship between the mechanical displacement amplitude and the temperature increase resulting from power absorbance.

The frequency tuning slope as a function of the pump power (i.e., the change in resonance frequency per unit of absorbed power) was used to characterize the photothermal sensitivity of the sensor. Considering the insertion losses associated with fiber optic lines, we measured the incident power with a Thorlabs PM320E optical power meter just prior to the fiber tip. An incident power absorption efficiency of 2.3% for single layer graphene[6] that scales up as the number of graphene layers increases was assumed.[33] On this basis, each 1 mW increase in the pump laser power provided an absorbed power increase of approximately 1.4 μW. The resonance frequency shift, Δf, as a function of the absorbed laser power increase, ΔP_{abs}, is shown in Figure 3d, in which the magenta triangles and red spheres indicate the first fundamental mode and second-order mode mechanical resonance frequency shifts due to photothermal absorption at room temperature, respectively. The corresponding photothermal sensitivities were calculated to be approximately 2.18 and 6.23 kHz/μW by applying a linear fit to these experimental data. The second-order frequency therefore exhibited a higher photothermal sensitivity compared with the first-order frequency at room temperature, indicating that

https://doi.org/10.1021/acsphotonics.1c01676
ACS Photonics 2022, 9, 1586−1593

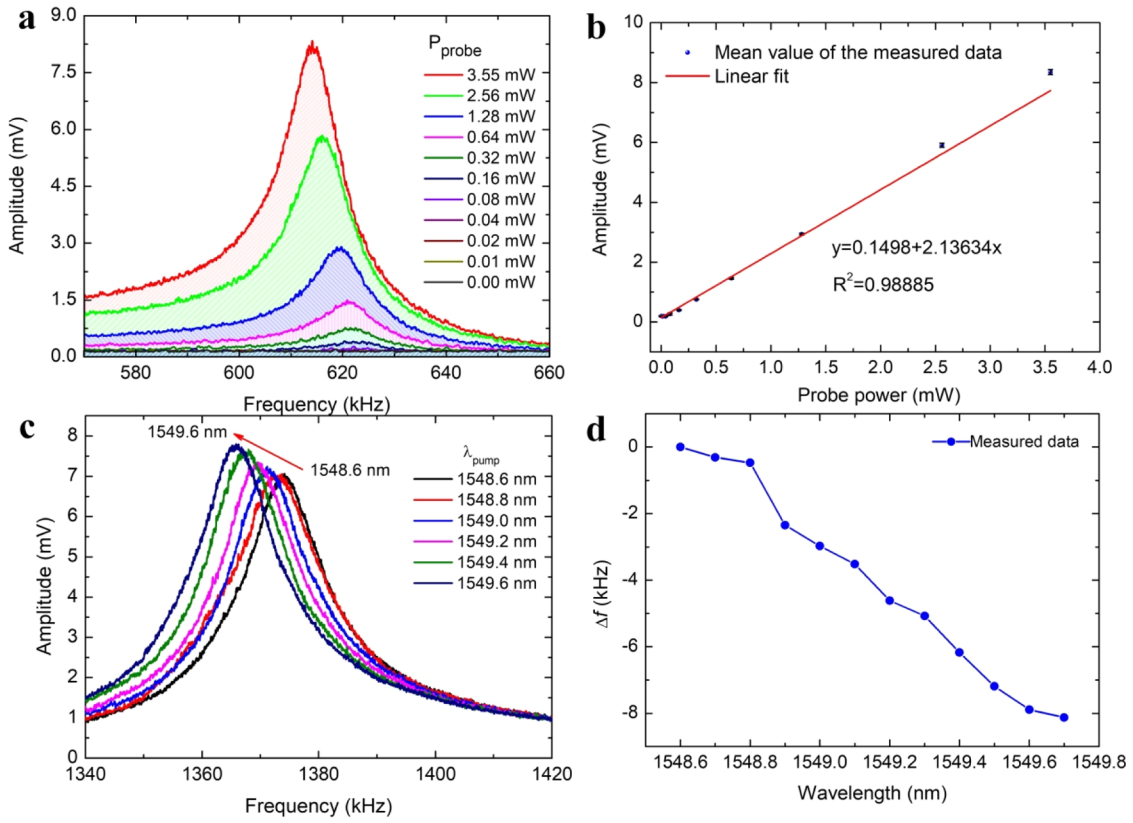

Figure 4. (a) Measured displacement noise amplitude as a function of probe power. (b) Variations in amplitude at f_1 as a function of different probe powers applied to the MLG. (c) Changes in mechanical resonance spectra of the trampoline-shaped GNB having a diameter of approximately 40 μm while varying the pump wavelength from 1548.6 to 1549.7 nm with a probe wavelength of 1530.2331 nm. (d) Frequency shifts obtained while varying the pump wavelength from 1548.6 to 1549.7 nm.

the sensitivity of our GNB resonator could potentially be improved by monitoring higher order modes. To exclude the effects of temperature fluctuations, we also assessed the photothermal response of the device at 0 °C by placing it in an ice water bath (see Supporting Information, Note 1). Similar to the prior room-temperature experiments, the second-order resonance frequency underwent a linear shift toward lower frequencies as the pump power was increased, as demonstrated by the dark diamonds in Figure 3d. The photothermal sensitivity was calculated to be 6.44 kHz/μW by applying a linear fit to the data. The photothermal sensitivities of the second-order frequency at room temperature and at 0 °C were on the same order of magnitude, confirming the sensitivity of this technique. These shifts to lower frequency values were primarily attributed to static changes in membrane tension resulting from laser heating.[34]

Notably, modest improvements in the performance of this system could be obtained by adjusting the electrical spectrum analyzer measurement bandwidth, which was set at 500 Hz in the present trials. By assessing frequency shifts of the sensor at values other than the absolute frequency, the sensor resonant frequency could be self-calibrated. Additionally, by focusing on the resonant frequency shifts as opposed to the absolute NOMS displacement, any effects of thermal-mechanical noise could be avoided because monitoring of the static deflection of the NOMS structure is limited by thermal-mechanical noise. Furthermore, the performance of the resonator (as reflected by its Q factor and photothermal sensitivity) could be further improved by using an optimized trampoline geometry incorporating a smaller tether width and longer tether length[6] or a tethered cantilever shape,[35] as reported previously. Lastly, ambient temperature has an effect on the resonator's performance (see the Supporting Information).

Figure 4a shows the shifts in the first-order fundamental resonance frequency, f_1, of the MLG resonator while increasing the probe power from 0 to 3.55 mW and with the pump power at a fixed value of 12 mW. The noise spectrum was essentially constant as the probe power was increased from 0 to 0.32 mW. At this low probe power, the noise was largely electrical noise rather than shot noise. However, with continued increases in the probe power of the laser, the total noise increased and eventually exceeded the electrical noise, indicating that the shot noise should be considered. Simultaneously, a larger SNR along with a smaller minimum detectable signal were achieved as the probe power increased. Figure 4b presents the amplitude of the resonance frequency at f_1 as a function of the probe power applied to the MLG. It is evident that the amplitude increased linearly as the probe power increased from 0 to 3.55 mW. The error bars, which represent plus/minus one standard deviation, were obtained by repeating each measurement three times.

Figure 4c summarizes changes in the mechanical resonance spectrum of the GNB as the pump laser wavelength was varied from 1548.6 to 1549.7 nm in 0.1 nm intervals while keeping the other key parameters fixed. These parameters included a pump power of 12 mW, probe wavelength of 1530.2331 nm, and probe power of 3.55 mW. A slight decrease in resonance frequency and a slight increase in the amplitude of the resonance frequency appeared as the pump wavelength was increased. However, as shown in Figure 4d, the resonance

https://doi.org/10.1021/acsphotonics.1c01676
ACS Photonics 2022, 9, 1586−1593

frequency did not exhibit a typical dip in the wavelength range of 1548.6−1549.7 nm, indicating that the GNB did not have a specific absorption band. Thus, the proposed sensor provided constant absorption of light across a wide range of wavelengths, which is in agreement with previous reported works.[34]

CONCLUSIONS

This work demonstrated a new type of all-optical-fiber bolometer comprising an optomechanical cavity resonator. This device was fabricated using a polymer-free direct transfer method to apply graphene to the fiber tip, following which the graphene was patterned into a trampoline geometry using an FIB and then micro-vacuum packaged. This structure provides several advantages, including a lack of organic residues, excellent crystallinity, and a high SNR. By monitoring the resonance frequency shifts induced by light absorption, we achieved photothermal sensitivities of approximately 2.18 kHz/μW for the first order mode at room temperature. The sensitivity of the aforementioned detection technique was improved by tracking the second-order resonance mode. Photothermal sensitivities of 6.23 and 6.44 kHz/μW were achieved at room temperature and 0 °C, respectively, demonstrating the high resolution of this technique. The proposed sensor is an all-fiber device and does not require electrical power on-chip or a vacuum chamber; thus, it could be used as a stand-off sensor in real-world applications. Furthermore, incorporating different functional materials could allow the proposed graphene-based NOMS resonator to serve as a platform for diverse chemical/physical measurements in the future. This technology is expected to find applications in areas such as medicine, industrial manufacturing, nanoscience, and astronomy.

METHODS

The fabrication of the fiber tip FP interferometer using MLG involved four steps (see Supporting Information, Note 3). Step 1 (Supporting Information, Figure S6a,b) employed a commercial MLG film comprising 10−15 layers (SixCarbon Tech., Shenzhen, China) grown on a copper foil having a thickness of 20 μm using chemical vapor deposition. In this step, the MLG film was detached from the Cu foil by a wet etching process in which the MLG/Cu sample was immersed in a 50 mg/mL aqueous $FeCl_3$ solution within a culture dish. In step 2 (Supporting Information, Figure S6c), after the Cu foil was fully etched away, the $FeCl_3$ solution was carefully removed and deionized (DI) water was added dropwise to the culture dish after which this wash water was removed. This washing process was repeated three or more times until the wash water was colorless to remove any residual ions. In step 3 (Supporting Information, Figure S6d), a section of a commercially available hollow core fiber (HCF) with an internal diameter of 40 ± 03 μm (Polymicro, TSP 040150) or 75 ± 03 μm (Polymicro, TSP 075150) was spliced onto a conventional single mode fiber (SMF, Corning Inc., SMF-28.) to form an open micro-cavity on the fiber end facet. A commercial fusion splicer (Fujikura, FSM-62S, slicing parameters: standard 25 bit, 400 ms) operated in the manual mode was used for the splicing, while a standard fiber cleaver in conjunction with a microscope was used for cleaving. Using these devices, an open micro-cavity having a length of L (adjustable between 10 and 70 μm) was created on the fiber end facet. A clean MLG film floating on a pool of DI water was then transferred onto the HCF to form an enclosed microscale air cavity. During this transfer process, the fiber was fixed on a translational stage with its tip facing the water and was slowly moved toward the MLG film. The fiber tip was immediately pulled up as soon as it touched the MLG. As a result of the surface tension of the water, the MLG (along with some residual water) adhered firmly onto the fiber tip. After the residual water was evaporated by allowing the resulting graphene-based device to dry naturally in a clean box at room temperature for more than 24 h, the MLG remained attached to the HCF end facet based on van der Waals forces. The graphene was thus suspended over the microscale air cavity to form an enclosed FP interferometer at the fiber tip (Supporting Information, Figure S6e). The graphene was subsequently shaped into a trampoline morphology using an FIB. An optical microscope image of the patterned graphene is provided in Supporting Information, Figure S6f. An ion sputtering instrument was used to apply a gold film over top of the MLG film with a coating time of 120 s to further enhance the reflectivity of the layer.

FIB Patterning into a Trampoline Morphology. The graphene was shaped into a trampoline geometry using an FIB (FEI Scios2 DualBeam) with a Ga^+ source, employing an ion beam current and a voltage of 0.1 nA and 30 kV, respectively. Four circular outlines centered on the circumference of the HCF were cut into the graphene drumhead to form the trampoline shape. A single beam pass with a dwell time of 1 μs was used for the cutting. A line was etched completely through the suspended graphene sheet by repeating this process three times. Owing to the high tension of the graphene sheet, the graphene inside the circular cut was collapsed into the cavity or curled up, while the remaining graphene sheet formed the trampoline morphology.

Micro-Vacuum Packaging Process. The vacuum micro-packaging of the MLG-based fiber-tip FP interferometer, which involved four steps, is shown in Supporting Information, Figure S7. First, one section of the SMF with the fiber tip sensor and one section of a silica capillary (250 ± 06 μm bore diameter) were placed in the left and right fiber holders in a carbon dioxide laser processing system, respectively, as shown in Supporting Information, Figure S7a. Second, the fiber tip sensor and the silica capillary were moved toward each other until the sensor was entirely inserted into the silica capillary and laser power was turned on with appropriate parameters for splicing a standard silica capillary. Consequently, the silica capillary was welded together, as shown in Supporting Information, Figure S7b. Third, the other end of the silica capillary was fused to another section of silica capillary that was affixed to a vacuum chamber (Supporting Information, Figure S7c). Lastly, as shown in Supporting Information, Figure S7d, applying a vacuum to the silica capillary (while monitoring the pressure using a vacuometer) caused the capillary to be natural fused while being welded together based on the input of the laser power. In this manner, the fiber tip graphene device was micro-vacuum packaged inside the capillary, in which the pressure was less than 5×10^{-6} mbar. Note that a small amount of strain was applied during the continuous laser heating of the device. An optical microscope image of the final packaged sensor is provided in Supporting Information, Figure S8.

https://doi.org/10.1021/acsphotonics.1c01676
ACS Photonics 2022, 9, 1586−1593

■ ASSOCIATED CONTENT

Supporting Information

The Supporting Information is available free of charge at https://pubs.acs.org/doi/10.1021/acsphotonics.1c01676.

Optomechanical system experimental setup, acquiring reflectance spectra, simulation, photothermal sensing results for first-order mechanical resonance frequency, frequency stability, device fabrication, and temperature measurement (PDF)

■ AUTHOR INFORMATION

Corresponding Author

Yiping Wang − *Key Laboratory of Optoelectronic Devices and Systems of Ministry of Education/GuangDong Province, College of Physics and Optoelectronic Engineering and Shenzhen Key Laboratory of Photonic Devices and Sensing Systems for Internet of Things, Guangdong and Hong Kong Joint Research Centre for Optical Fibre Sensors, Shenzhen University, Shenzhen 518060, China*; Email: ypwang@szu.edu.cn

Authors

Shen Liu − *Key Laboratory of Optoelectronic Devices and Systems of Ministry of Education/GuangDong Province, College of Physics and Optoelectronic Engineering and Shenzhen Key Laboratory of Photonic Devices and Sensing Systems for Internet of Things, Guangdong and Hong Kong Joint Research Centre for Optical Fibre Sensors, Shenzhen University, Shenzhen 518060, China*; orcid.org/0000-0001-9266-2498

Yanping Chen − *Key Laboratory of Optoelectronic Devices and Systems of Ministry of Education/GuangDong Province, College of Physics and Optoelectronic Engineering and Shenzhen Key Laboratory of Photonic Devices and Sensing Systems for Internet of Things, Guangdong and Hong Kong Joint Research Centre for Optical Fibre Sensors, Shenzhen University, Shenzhen 518060, China*

Huailei Lai − *Key Laboratory of Optoelectronic Devices and Systems of Ministry of Education/GuangDong Province, College of Physics and Optoelectronic Engineering and Shenzhen Key Laboratory of Photonic Devices and Sensing Systems for Internet of Things, Guangdong and Hong Kong Joint Research Centre for Optical Fibre Sensors, Shenzhen University, Shenzhen 518060, China*

Mengqiang Zou − *Key Laboratory of Optoelectronic Devices and Systems of Ministry of Education/GuangDong Province, College of Physics and Optoelectronic Engineering and Shenzhen Key Laboratory of Photonic Devices and Sensing Systems for Internet of Things, Guangdong and Hong Kong Joint Research Centre for Optical Fibre Sensors, Shenzhen University, Shenzhen 518060, China*

Hang Xiao − *Key Laboratory of Optoelectronic Devices and Systems of Ministry of Education/GuangDong Province, College of Physics and Optoelectronic Engineering and Shenzhen Key Laboratory of Photonic Devices and Sensing Systems for Internet of Things, Guangdong and Hong Kong Joint Research Centre for Optical Fibre Sensors, Shenzhen University, Shenzhen 518060, China*

Peijing Chen − *Key Laboratory of Optoelectronic Devices and Systems of Ministry of Education/GuangDong Province, College of Physics and Optoelectronic Engineering and Shenzhen Key Laboratory of Photonic Devices and Sensing Systems for Internet of Things, Guangdong and Hong Kong Joint Research Centre for Optical Fibre Sensors, Shenzhen University, Shenzhen 518060, China*

Bin Du − *Key Laboratory of Optoelectronic Devices and Systems of Ministry of Education/GuangDong Province, College of Physics and Optoelectronic Engineering and Shenzhen Key Laboratory of Photonic Devices and Sensing Systems for Internet of Things, Guangdong and Hong Kong Joint Research Centre for Optical Fibre Sensors, Shenzhen University, Shenzhen 518060, China*

Xunzhou Xiao − *Key Laboratory of Optoelectronic Devices and Systems of Ministry of Education/GuangDong Province, College of Physics and Optoelectronic Engineering and Shenzhen Key Laboratory of Photonic Devices and Sensing Systems for Internet of Things, Guangdong and Hong Kong Joint Research Centre for Optical Fibre Sensors, Shenzhen University, Shenzhen 518060, China*

Jun He − *Key Laboratory of Optoelectronic Devices and Systems of Ministry of Education/GuangDong Province, College of Physics and Optoelectronic Engineering and Shenzhen Key Laboratory of Photonic Devices and Sensing Systems for Internet of Things, Guangdong and Hong Kong Joint Research Centre for Optical Fibre Sensors, Shenzhen University, Shenzhen 518060, China*; orcid.org/0000-0002-9417-2019

Complete contact information is available at: https://pubs.acs.org/10.1021/acsphotonics.1c01676

Author Contributions

S.L. and Y.C. jointly conceived the idea. Y.C., H.L., S.L., P.C., and H.X. designed and fabricated the devices, built the experimental setup, and carried out the experiments. Y.C., S.L., B.D., X.X., and J.H. analyzed the data. S.L. and Y.W. assisted with the theory. M.Z. developed the modeling. Y.C. wrote the manuscript and S.L. edited the manuscript with contributions from all co-authors. All authors have given approval to the final version of the manuscript.

Funding

This study was supported by the National Natural Science Foundation of China (NSFC) (62175165 and 61905165); Guangdong Basic and Applied Basic Research Foundation (2021A1515011834); Foundation for Distinguished Young Talents in Higher Education of Guangdong (2018KQNCX219); and Shenzhen Science and Technology Program (grant nos. RCBS20200714114922296 and JCYJ20210324120403009).

Notes

The authors declare no competing financial interest.

■ ACKNOWLEDGMENTS

The authors wish to acknowledge the assistance on FIB received from the Electron Microscope Center of the Shenzhen University. We thank Liwen Bianji (Edanz) (https://www.liwenbianji.cn) for editing the language of a draft of this article.

■ REFERENCES

(1) Ghatge, M.; Walters, G.; Nishida, T.; Tabrizian, R. An ultrathin integrated nanoelectromechanical transducer based on hafnium zirconium oxide. *Nat. Electron.* **2019**, *2*, 506−512.

(2) Zhou, J.; Moldovan, N.; Stan, L.; Cai, H.; Czaplewski, D. A.; López, D. Approaching the Strain-Free Limit in Ultrathin Nanomechanical Resonators. *Nano Lett.* **2020**, *20*, 5693−5698.
(3) Zhang, X. C.; Myers, E. B.; Sader, J. E.; Roukes, M. L. Nanomechanical torsional resonators for frequency-shift infrared thermal sensing. *Nano Lett.* **2013**, *13*, 1528−1534.
(4) Barton, R. A.; Ilic, B.; van der Zande, A. M.; Whitney, W. S.; McEuen, P. L.; Parpia, J. M.; Craighead, H. G. High, size-dependent quality factor in an array of graphene mechanical resonators. *Nano Lett.* **2011**, *11*, 1232−1236.
(5) Kokkoniemi, R.; Girard, J.-P.; Hazra, D.; Laitinen, A.; Govenius, J.; Lake, R. E.; Sallinen, I.; Vesterinen, V.; Partanen, M.; Tan, J. Y.; Chan, K. W.; Tan, K. Y.; Hakonen, P.; Möttönen, M. Bolometer operating at the threshold for circuit quantum electrodynamics. *Nature* **2020**, *586*, 47−51.
(6) Blaikie, A.; Miller, D.; Alemán, B. J. A fast and sensitive room-temperature graphene nanomechanical bolometer. *Nat. Commun.* **2019**, *10*, 4726.
(7) Alemán, B.; Rousseas, M.; Yang, Y.; Regan, W.; Crommie, M.; Wang, F.; Zettl, A. Polymer-free, low tension graphene mechanical resonators. *Phys. Status Solidi RRL* **2013**, *7*, 1064−1066.
(8) Davidovikj, D.; Slim, J. J.; Cartamil-Bueno, S. J.; van der Zant, H. S. J.; Steeneken, P. G.; Venstra, W. J. Visualizing the Motion of Graphene Nanodrums. *Nano Lett.* **2016**, *16*, 2768−2773.
(9) Singh, R.; Sarkar, A.; Guria, C.; Nicholl, R. J. T.; Chakraborty, S.; Bolotin, K. I.; Ghosh, S. Giant Tunable Mechanical Nonlinearity in Graphene-Silicon Nitride Hybrid Resonator. *Nano Lett.* **2020**, *20*, 4659−4666.
(10) Jiang, C.; Li, Q.; Huang, J.; Bi, S.; Ji, R.; Guo, Q. Single-Layer MoS2 Mechanical Resonant Piezo-Sensors with High Mass Sensitivity. *ACS Appl. Mater. Interfaces* **2020**, *12*, 41991−41998.
(11) Manzeli, S.; Dumcenco, D.; Migliato Marega, G.; Kis, A. Self-sensing, tunable monolayer MoS2 nanoelectromechanical resonators. *Nat. Commun.* **2019**, *10*, 4831.
(12) Morell, N.; Tepsic, S.; Reserbat-Plantey, A.; Cepellotti, A.; Manca, M.; Epstein, I.; Isacsson, A.; Marie, X.; Mauri, F.; Bachtold, A. Optomechanical Measurement of Thermal Transport in Two-Dimensional MoSe2 Lattices. *Nano Lett.* **2019**, *19*, 3143−3150.
(13) Lu, R.; Li, Z.; Xu, G.; Wu, J. Z. Suspending single-wall carbon nanotube thin film infrared bolometers on microchannels. *Appl. Phys. Lett.* **2009**, *94*, 163110.
(14) Efetov, D. K.; Shiue, R.-J.; Gao, Y.; Skinner, B.; Walsh, E. D.; Choi, H.; Zheng, J.; Tan, C.; Grosso, G.; Peng, C.; Hone, J.; Fong, K. C.; Englund, D. Fast thermal relaxation in cavity-coupled graphene bolometers with a Johnson noise read-out. *Nat. Nanotechnol.* **2018**, *13*, 797−801.
(15) Itkis, M. E.; Borondics, F.; Yu, A.; Haddon, R. C. Thermal conductivity measurements of semitransparent single-walled carbon nanotube films by a bolometric technique. *Nano Lett.* **2007**, *7*, 900.
(16) Sansa, M.; Defoort, M.; Brenac, A.; Hermouet, M.; Banniard, L.; Fafin, A.; Gely, M.; Masselon, C.; Favero, I.; Jourdan, G.; Hentz, S. Optomechanical mass spectrometry. *Nat. Commun.* **2020**, *11*, 3781.
(17) Han, G.-R.; Jiang, J.-W. Edge-mode-based graphene nanomechanical resonators for high-sensitivity mass sensor. *Europhys. Lett.* **2018**, *123*, 36002.
(18) Kokkoniemi, R.; Govenius, J.; Vesterinen, V.; Lake, R. E.; Gunyhó, A. M.; Tan, K. Y.; Simbierowicz, S.; Grönberg, L.; Lehtinen, J.; Prunnila, M.; Hassel, J.; Lamminen, A.; Saira, O.-P.; Möttönen, M. Nanobolometer with ultralow noise equivalent power. *Commun. Phys.* **2019**, *2*, 124.
(19) Dolleman, R. J.; Houri, S.; Davidovikj, D.; Cartamil-Bueno, S. J.; Blanter, Y. M.; van der Zant, H. S. J.; Steeneken, P. G. Optomechanics for thermal characterization of suspended graphene. *Phys. Rev. B* **2017**, *96*, 165421.
(20) Zheng, B.-C.; Yan, S.-C.; Chen, J.-H.; Cui, G.-X.; Xu, F.; Lu, Y.-Q. Miniature optical fiber current sensor based on a graphene membrane. *Laser Photonics Rev.* **2015**, *9*, 517−522.
(21) Ma, J.; Jin, W.; Ho, H. L.; Dai, J. Y. High-sensitivity fiber-tip pressure sensor with graphene diaphragm. *Opt. Lett.* **2012**, *37*, 2493−2495.
(22) Pisana, S.; Braganca, P. M.; Marinero, E. E.; Gurney, B. A. Tunable nanoscale graphene magnetometers. *Nano Lett.* **2010**, *10*, 341−346.
(23) Liu, Z.-y.; Cao, H.-q.; Xu, F. Fiber-optic Lorentz force magnetometer based on a gold-graphene composite membrane. *Appl. Phys. Lett.* **2018**, *112*, 203504.
(24) Bunch, J. S.; van der Zande, A. M.; Verbridge, S. S.; Frank, I. W.; Tanenbaum, D. M.; Parpia, J. M.; Craighead, H. G.; Mceuen, P. L. Electromechanical Resonators from Graphene Sheets. *Science* **2007**, *315*, 490−493.
(25) Koppens, F. H. L.; Mueller, T.; Avouris, P.; Ferrari, A. C.; Vitiello, M. S.; Polini, M. Photodetectors based on graphene, other two-dimensional materials and hybrid systems. *Nat. Nanotechnol.* **2014**, *9*, 780−793.
(26) Freitag, M.; Low, T.; Xia, F.; Avouris, P. Photoconductivity of biased graphene. *Nat. Photonics* **2012**, *7*, 53−59.
(27) Lee, G.-H.; Efetov, D. K.; Jung, W.; Ranzani, L.; Walsh, E. D.; Ohki, T. A.; Taniguchi, T.; Watanabe, K.; Kim, P.; Englund, D.; Fong, K. C. Graphene-based Josephson junction microwave bolometer. *Nature* **2020**, *586*, 42−46.
(28) Cleland, A. N. Thermomechanical noise limits on parametric sensing with nanomechanical resonators. *New J. Phys.* **2005**, *7*, 235.
(29) Fong, K. C.; Schwab, K. C. Ultrasensitive and Wide-Bandwidth Thermal Measurements of Graphene at Low Temperatures. *Phys. Rev. X* **2012**, *2*, 039903.
(30) Herring, P. K.; Hsu, A. L.; Gabor, N. M.; Shin, Y. C.; Kong, J.; Palacios, T.; Jarillo-Herrero, P. Photoresponse of an electrically tunable ambipolar graphene infrared thermocouple. *Nano Lett.* **2014**, *14*, 901−907.
(31) Pruessner, M. W.; Park, D.; Stievater, T. H.; Kozak, D. A.; Rabinovich, W. S. Optomechanical Cavities for All-Optical Photothermal Sensing. *ACS Photonics* **2018**, *5*, 3214−3221.
(32) Zande, A. M. v. d.; Barton, R. A.; Alden, J. S.; Ruiz-Vargas, C. S.; Whitney, W. S.; Pham, P. H. Q.; Park, J.; Parpia, J. M.; Craighead, H. G.; McEuen, P. L. Large-Scale Arrays of Single-Layer Graphene Resonators. *Nano Lett.* **2010**, *10*, 4869−4873.
(33) Nair, R. R.; Blake, P.; Grigorenko, A. N.; Novoselov, K. S.; Booth, T. J.; Stauber, T.; Peres, N. M. R.; Geim, A. K. Fine Structure Constant Defines Visual Transparency of Graphene. *Science* **2008**, *320*, 1308.
(34) Barton, R. A.; Storch, I. R.; Adiga, V. P.; Sakakibara, R.; Cipriany, B. R.; Ilic, B.; Wang, S. P.; Ong, P.; McEuen, P. L.; Parpia, J. M.; Craighead, H. G. Photothermal self-oscillation and laser cooling of graphene optomechanical systems. *Nano Lett.* **2012**, *12*, 4681−4686.
(35) Miller, D.; Alemán, B. Shape tailoring to enhance and tune the properties of graphene nanomechanical resonators. *2D Mater.* **2017**, *4*, 025101.

https://doi.org/10.1021/acsphotonics.1c01676
ACS Photonics 2022, 9, 1586−1593